

**Emerging investigator series: Determination of biphasic  
core-shell droplet properties using aerosol optical tweezers**

Journal:	<i>Environmental Science: Processes &amp; Impacts</i>
Manuscript ID	EM-ART-04-2018-000166.R1
Article Type:	Paper
Date Submitted by the Author:	31-May-2018
Complete List of Authors:	Gorkowski, Kyle; Carnegie Mellon University, Center for Atmospheric Particle Studies Donahue, Neil; Carnegie Mellon University, Center for Atmospheric Particle Studies Sullivan, Ryan; Carnegie Mellon University, Center for Atmospheric Particle Studies

## Environmental Significance Statement

The morphology of atmospheric aerosol particles dictates their interactions with and effects on their environment, controlling their optical and cloud nucleation properties, and their heterogeneous reactivity. The new algorithm presented here enables direct measurements of the morphology of individual levitated droplets using aerosol optical tweezers. A full evaluation of the accuracy of the retrieved properties from the core and shell phases in biphasic droplets is presented. Phase-separated core–shell particles have recently been identified as prevalent morphologies in atmospheric aerosols, driving the need for further study of biphasic particles. This new methodology advances our ability to study and understand complex realistic aerosol systems directly relevant to atmospheric chemistry, by determining the morphology and phase properties of individual particles in real-time.

# 1 Emerging investigator series: Determination of biphasic core-shell 2 droplet properties using aerosol optical tweezers

3 Kyle Gorkowski,<sup>1</sup> Neil M. Donahue,<sup>1</sup> Ryan C. Sullivan<sup>1\*</sup>

4 <sup>1</sup>Center for Atmospheric Particle Studies, Carnegie Mellon University, Pittsburgh, PA

5 \*Corresponding Author: Ryan C. Sullivan; rsullivan@cmu.edu

## 7 Abstract

8 We present a new algorithm for the analysis of whispering gallery modes (WGMs)  
9 found in the cavity enhanced Raman spectra retrieved from optically tweezed droplets.  
10 Our algorithm improves the computational scaling when analyzing core-shell droplets  
11 (i.e. phase-separated or biphasic droplets) in the aerosol optical tweezers (AOT), making  
12 it computationally practical to analyze spectra collected at a few Hz over hours-long  
13 experiments. This enables the determination of the size and refractive index of both the  
14 core and shell phases with high accuracy, at 0.5 Hz time resolution. Phase-separated core-  
15 shell droplets are common morphologies in a wide variety of biophysical, colloidal, and  
16 aerosolized chemical systems, and have recently become a major focus in understanding  
17 the atmospheric chemistry of particulate matter. Our new approach reduces the number  
18 of parameters directly searched for, decreasing computational demands. We assess the  
19 accuracy of the diameters and refractive indices retrieved from a homogeneous or core-  
20 shell droplet. We demonstrate the performance of the new algorithm using experimental  
21 data from a droplet of aqueous glycerol coated by squalane. We demonstrate that a shell  
22 formation causes adjacent WGMs to split from each other in their wavenumber position  
23 through the addition of a secondary organic aerosol shell around a NaCl(aq) droplet. Our  
24 new algorithm paves the way for more in-depth physiochemical experiments into liquid-  
25 liquid phase separation and their consequences for interfacial chemistry – a topic with  
26 growing experimental needs for understanding the dynamics and chemistry of  
27 atmospheric aerosol particles, and in biochemical systems.

## 1. Introduction

Liquid-liquid phase separation is an important phenomenon in many areas of chemistry and biology due to the unique properties that result after phase separation. In biochemistry, liquid-liquid phase separation (LLPS) can be used as a purification or extraction process for biomolecules such as proteins, enzymes, and viruses.<sup>1-7</sup> The concentration of solutes resulting from LLPS can lead to the sequestering of toxic molecules or enhanced reaction rates.<sup>8</sup> In the environment, LLPS can dramatically change the near-surface concentrations of species, either enhancing or reducing their availability for multiphase chemistry.<sup>3,9</sup> For these reasons, accurate and direct measurements of LLPS are an important observational need in biochemistry, environmental chemistry, and atmospheric chemistry. This work uses the aerosol optical tweezers to probe LLPS of atmospheric aerosols, but the new analysis method presented is not limited to atmospheric systems.

The aerosol optical tweezers (AOT) has become a valuable technique to directly determine key physicochemical properties of individual aerosols including viscosity, diffusion coefficients, surface tension, morphology, optical properties, hygroscopic growth factors, phase transitions, and heterogeneous chemical reactivity.<sup>10-31</sup> In a typical AOT system, a droplet is optically trapped by a focused laser beam, which also induces a cavity enhanced Raman spectrum (CERS).<sup>27</sup> Accurate values for the droplet's size and refractive index are retrieved from the wavelengths of the resonant Raman modes—commonly called Whispering Gallery Modes (WGMs) or morphology dependent resonances—in the droplet.<sup>21,24,32</sup> The WGMs arise as Raman scattered light is amplified in a spherically symmetrical droplet at discrete combinations of size, refractive index, and wavelength while the optical trap holds the droplet in air, acting as a low-loss resonating cavity. These two basic measurements of size and refractive index combined with the stable trapping of a particle enable direct real-time studies of aerosol physical properties with unprecedented precision and accuracy on levitated droplets surrounded by gas. Most studies thus far have focused on homogeneous single-phase droplets so that the

1  
2  
3 56 existing data analysis algorithms developed by Preston and Reid can be employed.  
4  
5 57 However, there is evidence that a core-shell morphology is common in many aerosol  
6  
7 58 systems,<sup>7,19,24,27,33-40</sup> demanding an effective way to accurately retrieve physical properties  
8  
9 59 from spherically symmetrical core-shell droplets.<sup>23,24,27,40</sup> Core-shell morphologies  
10  
11 60 dramatically change the particle's interfacial chemistry and properties, thus altering its  
12  
13 61 interactions with radiation and reactive gases, its equilibration timescale with the gas-  
14  
15 62 phase, and its ability to uptake water. Water uptake is a critical component of direct light  
16  
17 63 scattering and also the activation of particles into cloud droplets and ice crystals.<sup>41-44</sup> Here  
18  
19 64 we present an efficient computational approach for retrieving the properties of core-shell  
20  
21 65 droplets that improves upon the methods we briefly described in Gorkowski et al.<sup>24</sup> and  
22  
23 66 rigorously test the accuracy of this new algorithm.

24  
25 67 WGMs are morphological resonances inside a spherical droplet that form a standing  
26  
27 68 wave around the droplet's circumference. Since WGMs depend on the morphology of the  
28  
29 69 droplet, they can be used to distinguish between a homogeneous droplet and a core-shell  
30  
31 70 droplet. Further, the lack of WGMs can indicate a non-spherical partially-engulfed  
32  
33 71 morphology.<sup>15,16,19,27,39</sup> However, studies of core-shell droplets have to-date been limited  
34  
35 72 to select cases with additional constraining information. A previous algorithm required  
36  
37 73 *a priori* WGM labels specifying the mode number, mode order, and electromagnetic wave  
38  
39 74 type (either transverse electric (TE) or transverse magnetic (TM)) for each WGM.<sup>45</sup>  
40  
41 75 Another way to constrain the fit is to assign the refractive index ( $n$ ) and chromatic  
42  
43 76 dispersion ( $dn/d\lambda$ ) of the core and shell *a priori*, and then fit the diameter of the core and  
44  
45 77 shell, and the WGM labels.<sup>23,39</sup> Clearly *a priori* knowledge of the droplet's properties is  
46  
47 78 not possible in many aerosol systems, especially realistic complex chemical systems.  
48  
49 79 Lastly, in our previous work we implemented an exhaustive direct search approach that  
50  
51 80 could fit an isolated set of WGMs with no additional constraints but which took 24 to 48  
52  
53 81 hours for each Raman spectral frame measured every 2 seconds.<sup>27</sup> This approach is too  
54  
55 82 computationally expensive to analyze AOT experimental datasets that are often acquired  
56  
57 83 over many hours. Here we present an improvement of our earlier algorithm that can now

1  
2  
3 84 fit an individual set of WGMs in one Raman frame in less than 10 minutes using a  
4  
5 85 personal computer. However, a typical AOT experiment lasting 6 hours generates 11,000  
6  
7 86 individual spectra, and so treating the entire experiment as a set of independent spectra  
8  
9 87 would still require approximately of 51 days to analyze. Since the spectra are not  
10  
11 88 independent, we use comprehensive fits of the WGMs in a small subset of the spectra to  
12  
13 89 then assign the WGM labels for the rest of the spectra collected, reducing the total  
14  
15 90 computation time to a day or less.

## 17 91 **2. Experimental**

### 19 92 **2.1 Whispering Gallery Mode Theory**

21 93 The solutions for Mie light scattering from homogeneous droplets and core-shell  
22  
23 94 droplets have been studied and used extensively.<sup>21,32,45-52</sup> Using Lorenz-Mie scattering  
24  
25 95 theory, we numerically solve for the whispering gallery modes, which are sharp  
26  
27 96 resonances in the broader Mie scattering band. We follow the solution form presented in  
28  
29 97 Bohren and Huffman,<sup>53</sup> and shown in the Supplemental Information. The WGM  
30  
31 98 resonances correspond to standing electromagnetic waves with an integral number of  
32  
33 99 wavelengths that form around the circumference of a spherically symmetrical droplet.  
34  
35 100 When the spherical symmetry is broken, the standing waves do not exist.

37 101 The WGM resonances occur when the denominator of the Mie scattering  
38  
39 102 coefficient vanishes. Therefore, to find the resonance position, we set the denominator  
40  
41 103 equal to zero and solve for the Mie size parameter ( $\chi$ ) given a refractive index ( $m$ ), mode  
42  
43 104 number ( $n$ ), and mode order ( $o$ ). The Mie size parameter is a dimensionless number  
44  
45 105 relating the circumference of the particle ( $\pi d_p$ ) to the wavelength ( $\lambda$ ) of the light:  $\chi = \pi d_p / \lambda$ .  
46  
47 106 The homogeneous case has an approximate analytical solution; however, we use this only  
48  
49 107 as a starting point for the numerical solution, as Preston and Reid<sup>21</sup> demonstrated that  
50  
51 108 this analytical approximation has significant errors in the resulting resonance position.  
52  
53 109 However, it is sufficient to constrain the mode order, which usually has a small integer  
54  
55 110 range of  $o = 1, 2, \text{ or } 3$  (higher mode orders are typically too faint to measure). Given the  
56  
57 111 mode order, we then solve Eqn. (1) for the transverse magnetic and Eqn. (2) for the

1  
2  
3 112 transverse electric resonances for a homogeneous sphere. The solution utilizes Riccati-  
4  
5 113 Bessel functions  $\xi_n$ ,  $\psi_n$ , and  $\chi_n$ , with a prime indicating the first derivative with respect to  
6  
7 114 the argument.

$$8 \quad 9 \quad 10 \quad 115 \quad 0 = m\psi_n(m\chi) \xi'_n(\chi) - \xi_n(\chi) \psi'_n(m\chi) \quad (1)$$

$$12 \quad 116 \quad 0 = \psi_n(m\chi) \xi'_n(\chi) - m\xi_n(\chi) \psi'_n(m\chi) \quad (2)$$

13  
14 117 For a core-shell system, the standing wave propagates in two distinct dielectric  
15  
16 118 materials, and the solution is very sensitive to both materials when the thickness of the  
17  
18 119 shell is comparable to the wavelength of the resonating light. For the core-shell solution,  
19  
20 120 we again set the scattering coefficient's denominator equal to zero. We then derive Eqn.  
21  
22 121 (3) for the transverse magnetic resonance and Eqn. (4) for the transverse electric  
23  
24 122 resonance. In the core-shell notation, we added subscripts for the shell (s) and core (c)  
25  
26 123 refractive index, the core radial fraction ( $f_c$ ), and the Mie size parameter ( $\chi$ ) is defined by  
27  
28 124 the shell diameter. The influence of the core is folded into two additional terms  $A_n$  and  $B_n$   
29  
30 125 which are defined in Eqns. (5) and (6).

$$31 \quad 32 \quad 126 \quad 0 = \xi_n(\chi)[\psi'_n(m_s\chi) - A_n \chi'_n(m_s\chi)] - m_s \xi'_n(\chi)[\psi_n(m_s\chi) - A_n \chi_n(m_s\chi)] \quad (3)$$

$$33 \quad 34 \quad 127 \quad 0 = m_s \xi_n(\chi)[\psi'_n(m_s\chi) - B_n \chi'_n(m_s\chi)] - \xi'_n(\chi)[\psi_n(m_s\chi) - B_n \chi_n(m_s\chi)] \quad (4)$$

$$35 \quad 36 \quad 37 \quad 128 \quad A_n = \frac{m_s \psi_n(m_s \chi f_c) \psi'_n(m_c \chi f_c) - m_c \psi'_n(m_s \chi f_c) \psi_n(m_c \chi f_c)}{m_s \chi_n(m_s \chi f_c) \psi'_n(m_c \chi f_c) - m_c \chi'_n(m_s \chi f_c) \psi_n(m_c \chi f_c)} \quad (5)$$

$$38 \quad 39 \quad 40 \quad 41 \quad 129 \quad B_n = \frac{m_s \psi_n(m_c \chi f_c) \psi'_n(m_s \chi f_c) - m_c \psi_n(m_s \chi f_c) \psi'_n(m_c \chi f_c)}{m_s \chi'_n(m_s \chi f_c) \psi_n(m_c \chi f_c) - m_c \psi'_n(m_c \chi f_c) \chi_n(m_s \chi f_c)} \quad (6)$$

42  
43  
44 130 To initialize the numerical solution for the core-shell WGMs, we start with a core  
45  
46 131 fraction of one and use the homogeneous solution. Then we incrementally decrease the  
47  
48 132 core fraction in variable step sizes of  $10^{-4}$  to  $10^{-8}$ . We decrease the step size when the  
49  
50 133 numerical solution results in a non-smooth change from the previous result.

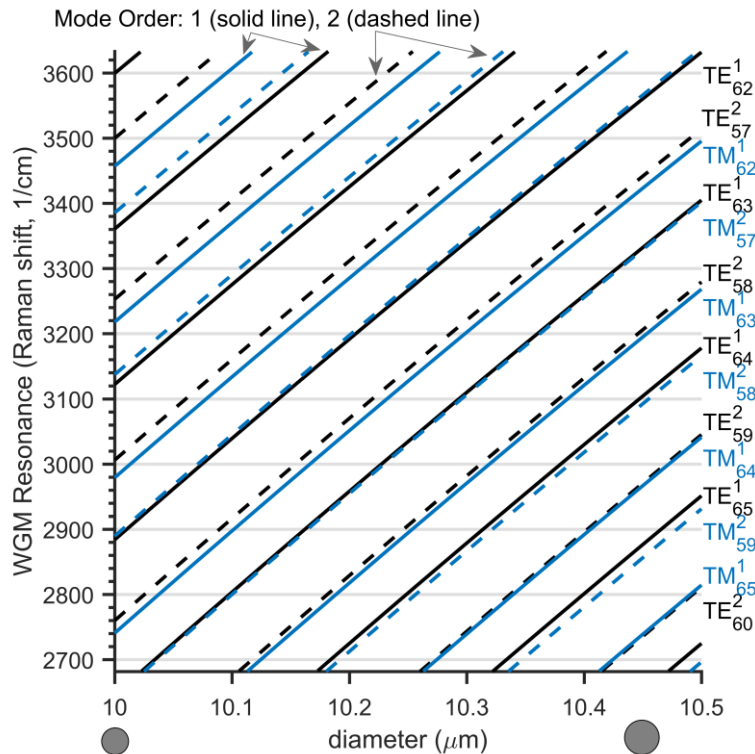
51  
52 134 Using the numerical solutions to Eqns. (1-6) we generate a database of Mie  
53  
54 135 resonances for both droplet morphologies. The homogeneous database returns a Mie  
55  
56  
57  
58  
59  
60

1  
2  
3 136 resonance given a refractive index ( $m$ ) and WGM label ( $l$ ), which corresponds to a specific  
4  
5 137 transverse electric or transverse magnetic resonance, mode number, and mode order. The  
6  
7 138 mode number corresponds to the number of standing wave nodes that are along the  
8  
9 139 interior surface of the droplet. The mode order corresponds to the number of standing  
10  
11 140 wave nodes in the radial direction from the surface of the droplet – these are essentially  
12  
13 141 higher order resonances. Either the electric or the magnetic field can be transverse,  
14  
15 142 indicating which field of the electromagnetic wave is propagating parallel to the droplet's  
16  
17 143 surface. The core-shell database returns a Mie resonance given a shell-refractive index  
18  
19 144 ( $m_s$ ), core-refractive index ( $m_c$ ), core-fraction ( $f_c$ ) and WGM label. The core-fraction  
20  
21 145 denotes where along the droplet's radial axis the refractive index changes between the  
22  
23 146 core and the shell phases. Refractive indexes change as a function of wavelength,  
24  
25 147 therefore to constrain the refractive index dependence on wavelength we use a chromatic  
26  
27 148 dispersion relation, Eqn. (7) following Preston and Reid,<sup>21</sup> where  $m_0$  is the refractive index  
28  
29 149 at a specified wavelength (typically 650 nm for a 532 nm trapping laser) and  $m_1$  is the  
30  
31 150 dispersion term which accounts for the wavelength dependence. This refractive index  
32  
33 151 dependence on wavelength is also used in the inverse fitting to constrain the fit as the  
34  
35 152 WGM positions are measured across a range of wavelengths.

$$36 \quad 153 \quad m_\lambda = m_0 + m_1 \left( \frac{1}{\lambda} - \frac{1}{\lambda_0} \right) \quad (7)$$

39 154 Using the database for the homogeneous case, we can generate WGM values  
40  
41 155 simulating different experimental conditions. Shown in Figure 1 is a simulation of single-  
42  
43 156 phase particle growth at a constant refractive index. As the droplet grows, the WGM  
44  
45 157 resonant frequencies increase in Raman-shift wavelength uniformly; the curves showing  
46  
47 158 the resonances are parallel in the Figure. Nearly overlapping WGMs will result in merged  
48  
49 159 peaks in the measured data, but this is not detrimental to the fitting. While for any given  
50  
51 160 pair of indices the WGMs progress in sequence (i.e.,  $TM^1_{62}$ ,  $TM^1_{63}$ ,  $TM^1_{64}$ ,...), the overall  
52  
53 161 sequence of all of the WGM labels at a given diameter is not universal because the relative  
54  
55 162 positions depend on refractive index. We show a similar plot to Figure 1 in the

1  
2  
3 163 Supplemental Information for refractive index and chromatic dispersion dependencies.  
4  
5 164 For a homogeneous droplet, the diameter is the most sensitive parameter to WGM  
6  
7 165 position, with a change of 0.66 nm in the retrieved  $d_p$  per 1  $\text{cm}^{-1}$  change in the WGM's  
8  
9 166 Raman shift. The refractive index ( $9.5 \times 10^{-5} (m_0)/\text{cm}^{-1}$ ) and a chromatic dispersion (0.004



36  
37 **Figure 1.** Calculated whispering gallery mode (WGM) positions as a  
38 homogeneous 10  $\mu\text{m}$  droplet grows by 500 nm in diameter, at a constant refractive  
39 index of 1.37. The WGM resonance wavelength is converted to a Raman shift from  
40 532 nm incident light, consistent with standard AOT experiments. Select WGM  
41 labels are indicated by TE for transverse electric (black) and TM for transverse  
42 magnetic (blue). The superscript is the mode order and the subscript is the mode  
43 number. Solid lines are mode order 1 and dashed lines are mode order 2.

45 167  $\mu\text{m}$  ( $m_1$ )/ $\text{cm}^{-1}$ ) are less sensitive. These sensitivities are the average slopes of the WGMs  
46  
47 168 across droplets of typical size and composition; see the Supplemental Information for  
48  
49 169 more details.

170 The parallel nature of the homogeneous WGM solutions shown in Figure 1 does  
 171 not translate to the core-shell WGMs. We generated core-shell WGM values simulating  
 172 the addition of a shell phase onto a core phase, shown in Figure 2. The WGM series do  
 173 not evolve in parallel because the different mode orders of the standing wave have a  
 174 different radial penetration depth and thus a different relative sensitivity to the dielectric  
 175 properties of the shell and the core. This broken symmetry is a strong identifying  
 176 characteristic of core-shell droplets. Mode order 1 is more sensitive to changes at the  
 177 droplet's outer surface where the shell resides than mode order 2 is, as this mode order  
 178 traverses more deeply into the droplet. The transverse electric WGMs have a sharper  
 179 radial intensity distribution than the transverse magnetic modes, which also contributes  
 180 to the non-parallel evolution. From Figure 2 we also observe that WGMs that were  
 181 overlapping in the homogeneous spectrum become resolvable because they split in their  
 182 Raman shift positions when the shell grows. This WGM peak splitting and non-parallel

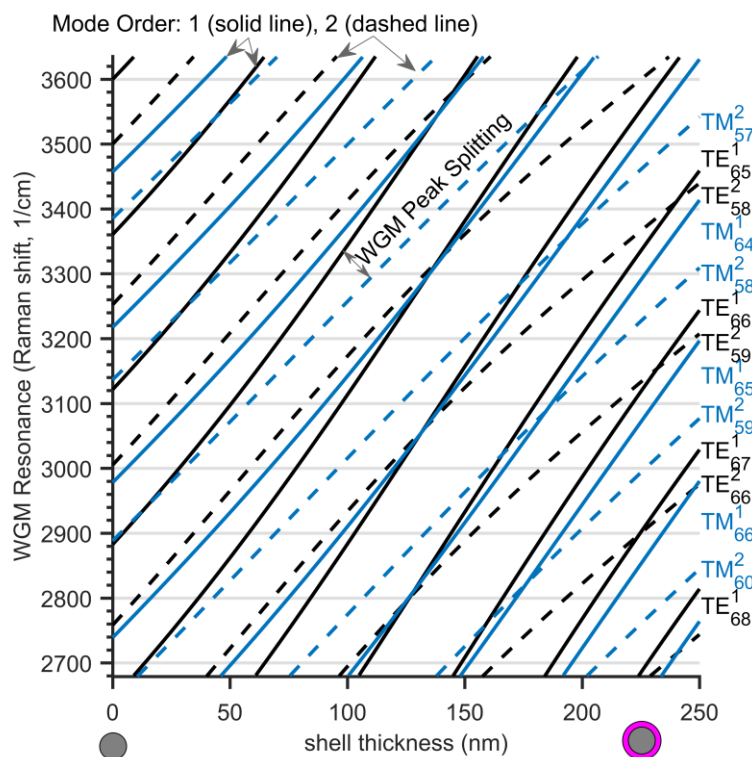


**Figure 2.** Calculated WGM positions for a core-shell droplet with a constant 10  $\mu\text{m}$  diameter core with a constant refractive index of 1.37, as in Fig. 1. Growth adds a shell with refractive index 1.45 and the thickness indicated on the x-axis. The WGM labels follow the same notation as Fig. 1.

1  
2  
3 183 WGM evolution with changing size are qualitative patterns that can be used to  
4  
5 184 distinguish core-shell WGMs from homogenous WGMs. More broadly, the non-parallel  
6  
7 185 evolution indicates a radial gradient in properties near the droplet surface with a length  
8  
9 186 scale of 10s to 100s of nm, smaller than the wavelength of the trapping laser.

## 11 187 **2.2 Inverse Algorithms for WGM Analysis: Overview**

13 188 We developed an inverse optimization algorithm that applies to both the  
14  
15 189 homogeneous and the core-shell morphology. The goal of the algorithm is to efficiently  
16  
17 190 and accurately match the WGM positions identified in the Raman spectrum to a specific  
18  
19 191 combination of diameter and refractive index using Mie theory. In this inverse problem  
20  
21 192 we are optimizing the diameter ( $d_p$ ), the refractive index ( $m_0$ ) along with dispersion ( $m_1$ )  
22  
23 193 as described in Eqn. 7, and the specific WGM labels ( $l$ ) as displayed in Figures 1 and 2.  
24  
25 194 We first describe existing algorithms and how the problem scales geometrically as the  
26  
27 195 number of parameters increases. We then preceded to outlining the optimization of a  
28  
29 196 single spectral frame of data, starting with how to internalize optimization of  $d_p$  and  
30  
31 197 therefore decrease the parameters directly searched for by one. We then discuss how the  
32  
33 198 combinations of discrete WGM labels are found. Lastly, we present the procedure for  
34  
35 199 optimization of the refractive index parameters ( $m_0$ , and  $m_1$ ). We then take another step  
36  
37 200 back and discuss how we can use a full time series of WGMs to further constrain each  
38  
39 201 WGM label ( $l$ ). As finding the optimum set of WGM labels constitutes a large fraction of  
40  
41 202 the computational time, avoiding this attribution for most data frames makes the analysis  
42  
43 203 significantly more efficient.

## 44 204 **2.3 Algorithm Optimization**

46 205 Existing algorithms for WGM analysis of homogeneous droplets are a  
47  
48 206 combination of direct search and least-squares minimization.<sup>21,23,32,54</sup> In a direct search the  
49  
50 207 computation scales as the number of parameters ( $d_p$ ,  $m_0$ ,  $m_1$ , and  $l$ ); for a homogeneous  
51  
52 208 droplet that is  $n^4$  for a single spectral frame ( $n_{frame}$ ). An improvement to this was first  
53  
54 209 proposed by Preston and Reid<sup>32</sup>. Their algorithm uses a low-resolution search and  
55  
56 210 subsequent refinement using an R-squared minimization. This results in a scaling of

211 approximately  $(n^3+1)n_{frame}$ , resulting in a one-second fit time per frame. To extend to a  
 212 core-shell parameter space using a fully direct search across all the fit parameters would  
 213 result in a  $(n^7)n_{frame}$  scaling ( $d_p, f_c, m_{C0}, m_{C1}, m_{S0}, m_{S1}$ , and  $l$ ). Our initial implementation of  
 214 this direct search resulted in a fit time of 24 to 48 hours per frame using a personal  
 215 computer depending on step size and parameter ranges, making this approach  
 216 unrealistic even if performed on a cluster. This geometric scaling of the direct search  
 217 algorithm makes the core-shell implementation unfeasible to analyze experimental data  
 218 sets routinely, as  $n_{frame}$  can typically exceed 10,000.

219 Our algorithm overcomes this computational challenge through three  
 220 innovations. First, we internalize the  $d_p$  search via the Mie size parameter ( $\chi = \pi d_p / \lambda$ ) so  
 221 that it is now an internal constraint, thus decreasing the scaling by one factor. Second, we  
 222 employ a random search ( $n_{rand}$ ) over  $f_c, m_{C0}, m_{C1}, m_{S0}$ , and  $m_{S1}$  to find possible sets of WGM  
 223 labels ( $n_{pWGM}$ ). Third, we take the individual WGMs and group them temporally into  
 224 WGM sequences ( $n_{seq}$ ), such that each sequence has a single WGM label (see the  
 225 Supplemental Information for an example). This results in an approximate single-frame  
 226 scaling for a homogeneous droplet of  $(n_{rand}n_{seq}+n^2)n_{pWGM}$  and for a core-shell droplet of  
 227  $(n_{rand}n_{seq}+n^5)n_{pWGM}$ . Once the labels are known for each of the  $n_{groups}$  then the scaling for  
 228 the time series is  $n^2n_{frame}$  for homogeneous droplets and  $n^5n_{frame}$  for core-shell droplets.  
 229 The resulting fit time for the homogeneous case is 2.6 seconds per frame for unlabeled  
 230 WGMs and 9 ms per frame for labeled WGMs. For the core-shell case, it is 6.8 minutes  
 231 per frame for unlabeled WGMs and 0.57 seconds per frame for labeled WGMs. We  
 232 provide an outline of the complete algorithm in the Supplemental Information.

## 233 2.4 Fitting a Single Raman Spectrum

234 Our first efficiency gain was to convert  $d_p$  into an internal constraint. This uses the  
 235 Mie size parameter ( $\chi$ ) to relate the given WGM positions to each other. As  $d_p$  can be  
 236 assumed to be constant in a single spectral frame the positions of the first WGM ( $\lambda_1$ ) can  
 237 be related to another WGM ( $\lambda_i$ ) as shown in Eqn. (8), where  $\chi_i$  is the Mie resonance for  
 238 the  $i^{\text{th}}$  WGM, and  $\chi_1$  is a possible Mie resonance for the first WGM.

$$\chi_i = \frac{\lambda_1}{\lambda_i} \chi_1 \quad (8)$$

240 The possible values for  $\chi_1$  are determined by the search space of WGM labels ( $l$ );  
 241 in this way, we constrain the range of possible  $d_p$ . This approach is very sensitive to the  
 242 accuracy of the initial  $\lambda_1$ , which can be the location of any of the observed WGMs.  
 243 Consequently, we initialize the search with several  $\lambda_i$  values, up to the full set of observed  
 244 WGMs. In practice, a comprehensive search showed no systematic improvements over  
 245 using only the first WGM, but to be cautious we initialize the search with the three largest  
 246 amplitude WGMs. This method of relating one Mie resonance to another internalizes the  
 247 diameter constraint so that we only need to search across the possible WGM label  
 248 combinations.

249 The number of possible WGM labels combinations does not need to be exhaustive  
 250 as we only need to track the best possible combinations. Consequently, we initiate the  
 251 search with random values for  $m_0$  and  $m_1$  for a homogeneous droplet, or for  $m_{s0}$ ,  $m_{s1}$ ,  $m_{c0}$ ,  
 252  $m_{c1}$  for core-shell droplets, and using a direct search for  $f_c$ . Then for each random guess  
 253 we start with all possible WGM labels for the first WGM,  $l_1$ , and then sequentially find  
 254 the best label for the next WGM in the measured spectrum. The minimization for the next  
 255  $l_i$  follows by calculating the squared error for each possible  $l$  by setting Eqn. (8) equal to  
 256 zero and squaring the result to get Eqn. (9). To account for neighboring WGM peaks, we  
 257 keep the 3-5 closest WGM labels that minimize the squared error. We then repeat this  
 258 process for the next WGM, etc. After a set number ( $i$ ) of such WGM searches we remove  
 259 a fraction (0.5 to 0.8) of the poorest WGM label sets to reduce the computational load;  
 260 however, we keep a minimum of 100 WGM label sets. Consequently, the WGM sets that  
 261 result in a high error are rapidly removed and are not propagated through the rest of the  
 262 computation. This process results in the 100 best possible WGM-label sets for a given  
 263 random guess. The random guess is then repeated until the probability of finding a new  
 264 and unique WGM-label set is less than 0.25%. For a homogeneous system, we average

213 unique WGM-label sets and for a core-shell system we average 488 unique WGM-label sets.

We then globally optimize each of the possible WGM label sets across their droplet properties:  $m_0$  and  $m_1$  for a homogeneous droplet and  $m_{S0}$ ,  $m_{S1}$ ,  $m_{C0}$ ,  $m_{C1}$ , and  $f_c$  for a core-shell droplet. The global optimization proceeds in two steps. The first is a gridded minimization finding the minimum based on the squared error of the Mie-size parameter:

$$\text{squared error} = \sum_{i=2}^{WGM \text{ count}} \left( \frac{\lambda_1}{\lambda_i} \chi_1 - \chi_i \right)^2 \quad (9)$$

We use a gridded search because the error landscape is non-smooth and non-convex with multiple local minima. We tested multiple gradient descent and global search algorithms, but to achieve reliable results they required more computational time than the simpler gridded search algorithm. We achieved an efficient gridded search for the many WGM-label combinations and higher dimensional parameter space in the core-shell fit using GPU computations instead of CPU computations as we found that a 4-core CPU desktop with a GPU was 39% faster than a cluster of 32 CPUs.

After we complete an initial global search we carry out a local refinement of the putative optimal solution using a gradient decent algorithm optimizing the reduced chi-squared value ( $\chi^2_{red}$ ) of the retrieved diameters ( $d_i$ ) calculated from the Mie size parameter, shown in Eqn. (10). We find the optimal diameter ( $\bar{d}_p$ ) by taking the average of each  $d_i$  calculated from each Mie size parameter. We propagate the measurement error ( $\sigma_i$ ) from the Gaussian fit of the WGM resonance peak in the spectrum.

$$\chi^2_{red.} = \frac{1}{WGM \text{ count} - \text{variable count}} \sum_{i=1}^{WGM \text{ count}} \left( \frac{d_i - \bar{d}_p}{\frac{\chi_i \sigma_i}{2\pi}} \right)^2 \quad (10)$$

The optimum WGM-label set can now be found by ranking the retrieved  $\chi^2_{red}$  for each WGM-label set. From simulation results shown in Figure 3 the optimum WGM-label set is not always the correct one. Near the optimum each of the WGM-label sets tends to

1  
2  
3 289 only have one or two WGMs of differing labels, leading to a multiple minimum with  
4  
5 290 similar physical properties. To account for that we use multiple Raman spectral frames  
6  
7 291 containing the same WGM sequences, which is described below, or we take an average  
8  
9 292 result of the multiple minima. This averaged result is the mean of all WGM-label sets that  
10  
11 293 have a  $\chi^2_{red}$  error that is lower than the lowest  $\chi^2_{red}$  error plus a  $1\sigma$  critical value. This  $1\sigma$   
12  
13 294 critical value is based on the degrees of freedom and the cumulative probability of a chi-  
14  
15 295 squared distribution. For a homogeneous optimization, this  $1\sigma$  critical value is 3.5 and for  
16  
17 296 a core-shell optimization it is 7.0. We call this type of fitting the  $1\sigma$  WGM labeled fit. This  
18  
19 297 final averaging step in the  $1\sigma$  WGM labeled fit increases the error in the fit but tends to  
20  
21 298 gain a more self-consistent result because it averages the degenerate solutions caused by  
22  
23 299 overlapping WGM labels.

## 24 300 **2.5 Fitting a Full Raman Spectral Time Series**

26 301 The last improvement to the optimization algorithm is to sort the individual  
27  
28 302 WGMs into sequences. This process starts with the first frame of WGMs and places  
29  
30 303 neighboring WGMs in the next frame into sequences based on the previous frame. If there  
31  
32 304 is no sequence within the variable threshold (typically 0.2 nm), then that individual WGM  
33  
34 305 creates a new sequence. This process is then repeated for the full experiment resulting in  
35  
36 306 100s to 1000s of WGM sequences; an example is shown in the Supplemental Information.  
37  
38 307 The labeling of the WGM sequences follows the same random search process as described  
39  
40 308 above, but in this case we average the  $\chi^2_{red}$  value across multiple Raman spectra that  
41  
42 309 contain the same set of WGM sequences, and therefore the same WGM-label sets. This  
43  
44 310 averaging of  $\chi^2_{red}$  helps resolve which WGM within the  $1\sigma$  WGM labeled fit has a  
45  
46 311 consistently low error across multiple frames and is thus more likely the correct label. For  
47  
48 312 this averaging to be effective we typically use 10 frames for a homogeneous system and  
49  
50 313 50 frames for a core-shell system. Even with this averaging of multiple frames there are  
51  
52 314 sometimes still multiple WGM-label sets within the  $1\sigma$  critical value – this is where our  
53  
54 315 algorithm can misidentify a WGM label due to it being too close to another WGM. Further  
55  
56 316 work in incorporating additional information into the algorithm is being pursued, such as

1  
2  
3 317 using the peak amplitude to constrain the possible WGM labels (TM peaks tend to be  
4  
5 318 smaller than TE peaks) and using the initial fit to find additional WGMs of lower  
6  
7 319 amplitude in the Raman spectrum.

8  
9 320 Once the WGM series all have a WGM label, then we fit the full time series using  
10  
11 321 the previously discussed global optimization of  $m_0$ ,  $m_1$ , and  $d_p$  for a homogeneous droplet  
12  
13 322 and of  $m_{S0}$ ,  $m_{S1}$ ,  $m_{C0}$ ,  $m_{C1}$ ,  $d_p$  and  $f_c$  for a core-shell droplet. Since fitting a set of core-shell  
14  
15 323 WGMs is much faster if the WGM labels are known, fitting the full time series can be  
16  
17 324 achieved when the WGMs are grouped into sequences. Using the WGM sequences results  
18  
19 325 there are fewer unlabeled fits that need to be completed.

20  
21 326

## 22 23 24 327 **3. Results and Discussion**

### 25 26 328 **3.1 Assessment of Algorithm's Performance**

27  
28 329 To assess our new inverse fitting algorithm, we generated WGM positions for a  
29  
30 330 simulated droplet and then added random Gaussian noise to the individual WGM  
31  
32 331 positions. Our random noise used a sigma of 0.01 nm, shown by Preston and Reid<sup>21</sup> to be  
33  
34 332 typical for measured WGMs and consistent with the uncertainty of the Raman  
35  
36 333 spectrograph used (Princeton Acton). We simulated all possible WGM labels up to mode  
37  
38 334 order 2 between 620 nm and 660 nm, which is representative of our typical Raman  
39  
40 335 spectrum acquisition using a 532 nm trapping laser and a 1200 grooves/mm diffraction  
41  
42 336 grating.<sup>24,27</sup> After finding all possible WGMs, we randomly selected a subset to use in the  
43  
44 337 fit. We progressively added WGMs to the initial random set to probe how the uncertainty  
45  
46 338 changes with the number of WGMs used in the fit. We then repeated this process 300  
47  
48 339 times by generating a new set of droplet properties randomly, based off of our typical  
49  
50 340 range of observed parameters (these are listed in the Supplemental Information). This  
51  
52 341 means that each simulation is a new droplet with a diameter between 9  $\mu\text{m}$  to 11  $\mu\text{m}$  and  
53  
54 342 a refractive index between 1.37 to 1.42. For this assessment, we used the algorithm to fit  
55  
56 343 a single Raman spectrum (frame) and did not incorporate any time evolution in the fit.

344 We describe the details of the simulation bounds as well as a comparison of computation  
 345 times in the Supplemental Information.

346 Using the simulation results we determined whether the calculated (presumably  
 347 global) minimum fit gave the known correct WGM-label set. We also determined whether  
 348 the correct WGM label set was within the  $1\sigma$  critical value of the global  $\chi^2_{red}$  minimum  
 349 (defined above) regardless of whether it was the optimal fit. We show these two cases in  
 350 Figure 3 for both a homogeneous and a core-shell droplet. The solid curves in Figure 3  
 351 indicate that the correct WGM label is not always at the minimum, but that the probability  
 352 rises with the number of WGMs used in the fit. This result is less of a concern for a  
 353 homogeneous droplet as there are usually more than 4 WGMs in a typical spectrum,  
 354 where the attribution accuracy is over 95%. However, for the core-shell droplet the

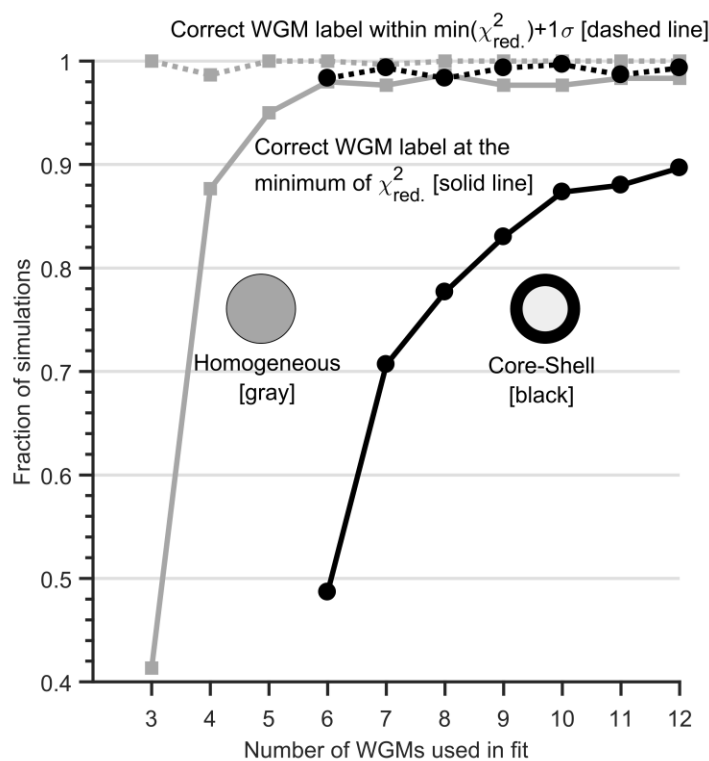


**Figure 3.** WGM labeling results for simulated droplets with a homogeneous (gray) or core-shell (black) morphology. The fraction of simulated fits that had the correct WGM label set at the minimum  $\chi^2_{red}$  error is shown with a solid line. The fraction of simulated fits that had the correct WGM label set within the minimum  $\chi^2_{red}$  error plus  $1\sigma$  is shown with a dashed line.

1  
2  
3 355 additional fit parameters increase the degeneracy in fitting incorrect WGM labels and the  
4  
5 356 attribution accuracy remains below 90% for even 12 WGMs. The increased probability  
6  
7 357 for the minimum of a core-shell droplet to be incorrectly labeled is why we implemented  
8  
9 358 the  $1\sigma$  critical range of the global  $\chi^2_{red}$  minimum. Figure 3 also shows that the correct  
10  
11 359 WGM-label set is near the minimum even if it is not at the minimum due to noise added  
12  
13 360 and the inherent flexibility in the model. That is one reason why we implemented WGM  
14  
15 361 grouping as it helps resolve which WGM label is consistently the minimum across  
16  
17 362 multiple measured spectra.

18  
19 363 Using the simulated WGMs and their resulting fits we assessed the error in the  
20  
21 364 resulting droplet parameters retrieved by the algorithm: diameter ( $d_p$ ) and refractive  
22  
23 365 index ( $m$ ). We examined two cases: (1) with the correct WGM label assignments what is  
24  
25 366 the global minimum (solid lines); and (2) for all fit results that are within the  $1\sigma$  critical  
26  
27 367 range of the global  $\chi^2_{red}$  minimum (dashed lines), what is the average error. The first case  
28  
29 368 applies if, by using multiple measured spectra (frames), we can determine which WGM  
30  
31 369 label set is the most consistent, and therefore correct. The second case quantifies the  
32  
33 370 variability in the  $1\sigma$  range of the global  $\chi^2_{red}$  minimum. We report the error of the fitting  
34  
35 371 as the standard deviation of the difference between the simulated parameter and the  
36  
37 372 resulting fitted parameter. In Figure 4 we show the error in droplet diameter as a function  
38  
39 373 of WGMs used. The error in the homogeneous droplet is consistent with the algorithm  
40  
41 374 developed by Preston and Reid<sup>21</sup>, which achieved  $\pm 2.2$  nm when fitting 12 WGMs. We  
42  
43 375 now provide an error assessment of the core and shell diameters. Our error in the shell  
44  
45 376 diameter (the total droplet diameter) is similar in magnitude to the homogeneous case,  
46  
47 377 but the error in the core diameter (total diameter – shell thickness) is significantly higher.  
48  
49 378 We attribute the increased error to the additional flexibility in the core-shell model. For  
50  
51  
52  
53  
54  
55  
56  
57  
58  
59  
60

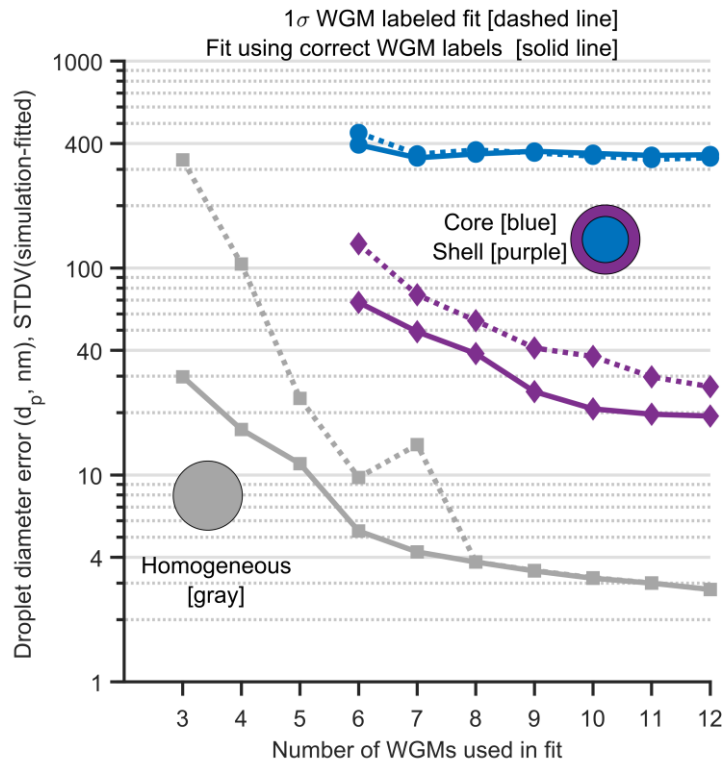


**Figure 4.** The fit error of a droplet's retrieved diameter ( $d_p$ ) in a homogeneous or core-shell droplet versus the number of WGMs used in the fit. The error is the standard deviation of 300 simulated droplets with a  $d_p$  between 9  $\mu\text{m}$  to 11  $\mu\text{m}$  at each set of WGMs used. The solid line is the minimum using the correct WGM labels. The dashed line represents the mean radius of the multiple minimums in the fits with a cut-off value of being everything within  $1\sigma$  of the global minimum.

379 experimental systems we try to fit data with at least 2 more WGMs than the minimum  
 380 required. For a homogeneous droplet this means 5 or more WGMs, and for core-shell  
 381 droplet this means 8 or more WGMs. Using that minimum threshold, we then averaged  
 382 across the remaining fits to get a typical error for any one experiment, this is tabulated in  
 383 the Supplemental Information. The fractional (percent) error of the various parameters  
 384 puts them into context; for a homogeneous particle, the fractional error in  $d_p$  is 0.045%  
 385 and for a core-shell particle, the fractional error in  $d_{shell}$  is 0.024% and the fractional error  
 386 in  $d_{core}$  is 3.8%. When we fit experimental data we know the initial diameter of the  
 387 homogeneous droplet and this helps to constrain the possible diameters of the core-shell  
 388 fit once the outer shell phase has formed or been added.

389 We evaluated the error in retrieving the refractive index using the same procedure.  
 390 Our refractive index dispersion model has two fit parameters to account for the small  
 391 change in refractive index as a function of wavelength. In Figure 5 we plot the error in  
 392 the first parameter,  $m_0$ , which for our simulation is equivalent to the refractive index at  
 393 650 nm,  $m_{650\text{ nm}}$ . We typically use  $m_{650\text{ nm}}$  as that corresponds to our WGM observations of  
 394 the broad O–H Raman mode with a Raman shift value of  $\sim 3400\text{ cm}^{-1}$ . The dispersion term  
 395 ( $m_1$ ) plays a necessary, yet minor role compared to  $m_0$  and  $d_p$ . We provide a plot of the  
 396 error in the dispersion term in the Supplemental Information. The error in the refractive  
 397 index for the homogeneous droplet is consistent with Preston and Reid,<sup>21</sup> which achieved  
 398  $\pm 0.00033$  with 12 WGMs. In the case of the core–shell droplet, after nine WGMs the level

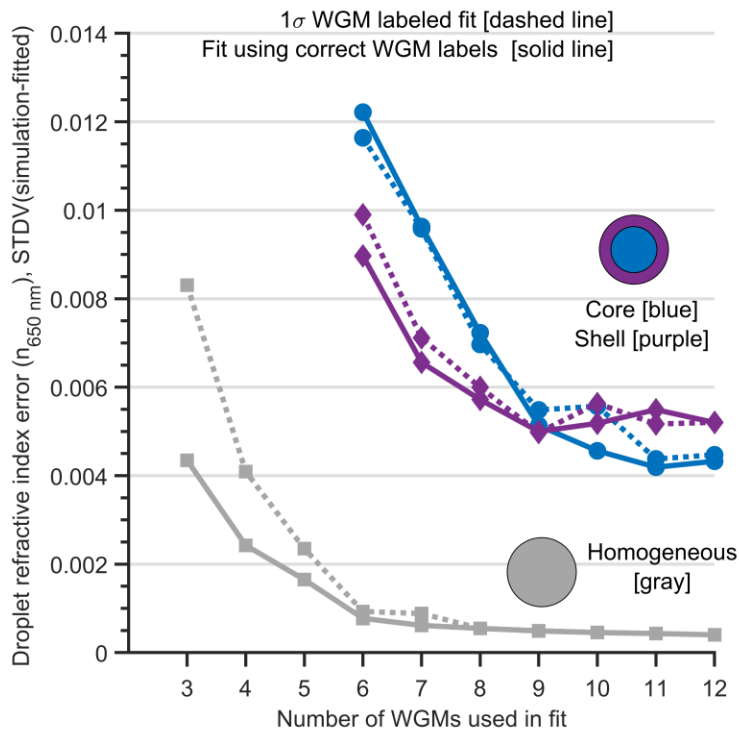


**Figure 5.** The refractive index ( $m_0$ ) fit error of a homogeneous and core-shell droplet's WGMs versus the number of WGMs used. The error is the standard deviation (STDV) of 300 simulated droplets with a  $m_0$  between 1.37 to 1.42 (homogeneous) at each set of WGMs used. The core-shell droplet had a  $m_{C0}$  between 1.37 to 1.42 and  $m_{S0}$  of 1.40 to 1.45. The solid line is the minimum using the correct WGM labels. The dashed line represents the mean radius of the multiple minimums in the fits with a cut off value of being everything within  $1\sigma$  of the global minimum.

1  
2  
3 399 of improvement in the fit with each additional WGM diminishes. We interpret this as a  
4  
5 400 minimum error asymptotic limit determined by the simulated noise added to the WGM  
6  
7 401 positions. Some future improvements could incorporate the amplitude of the WGM as  
8  
9 402 well as the width of the WGM as additional information, which may further improve the  
10  
11 403 fit accuracy.

12  
13 404 So far we have focused on simulations of data from the O-H Raman scattering  
14  
15 405 band. In some cases (i.e. a hydrophilic hydrocarbon shell) only the C-H Raman band  
16  
17 406 shows significant features. There are limitations to the fitting of WGMs when only the C-  
18  
19 407 H Raman scattering band common to organic carbon phases is measured (much narrower  
20  
21 408 than the broad O-H Raman mode for H<sub>2</sub>O), leading to fewer WGMs available for the  
22  
23 409 fitting.<sup>24,27</sup> To still gain some insight into the pure organic carbon systems we use *a priori*  
24  
25 410 information on the refractive index of the core phase to reduce the size of the feasible  
26  
27 411 parameter space, but even then the fits are not as well constrained as fits for systems with  
28  
29 412 the much broader O-H Raman signal present in aqueous phases.

### 30 413 **3.2 Spectral Response from Adding a Shell of Organic Carbon to an Aqueous** 31 32 414 **Inorganic Droplet**

33  
34 415 We use the addition of  $\alpha$ -pinene secondary organic aerosol (SOA) (formed by gas-  
35  
36 416 phase ozonolysis of  $\alpha$ -pinene vapor) to an NaCl(aq) droplet to explore how the droplet's  
37  
38 417 Raman spectrum and WGMs transition from a homogeneous droplet to a core-shell  
39  
40 418 droplet when a second phase (the SOA) is added.<sup>24</sup> This experiment, shown in Figure 6,  
41  
42 419 clearly demonstrates how the homogeneous fit becomes unrealistic for a core-shell  
43  
44 420 droplet after just a thin shell forms on the droplet. Figure 6 also shows the WGM peak  
45  
46 421 splitting caused by the growth of a shell on a previously homogeneous core as predicted  
47  
48 422 from the theoretical results shown in Figure 2. The experiment began with a trapped  
49  
50 423 NaCl(aq) droplet at roughly 75% RH. We then flowed ozone (3.4 ppm) and  $\alpha$ -pinene  
51  
52 424 vapor (182 ppm) into the chamber, forming SOA at t=0 minutes. The experimental  
53  
54 425 methods are described in the Supplemental Information, and in Gorkowski et al.<sup>24</sup> The  
55  
56 426 majority of the SOA shell growth was caused by coagulation of submicron SOA particles

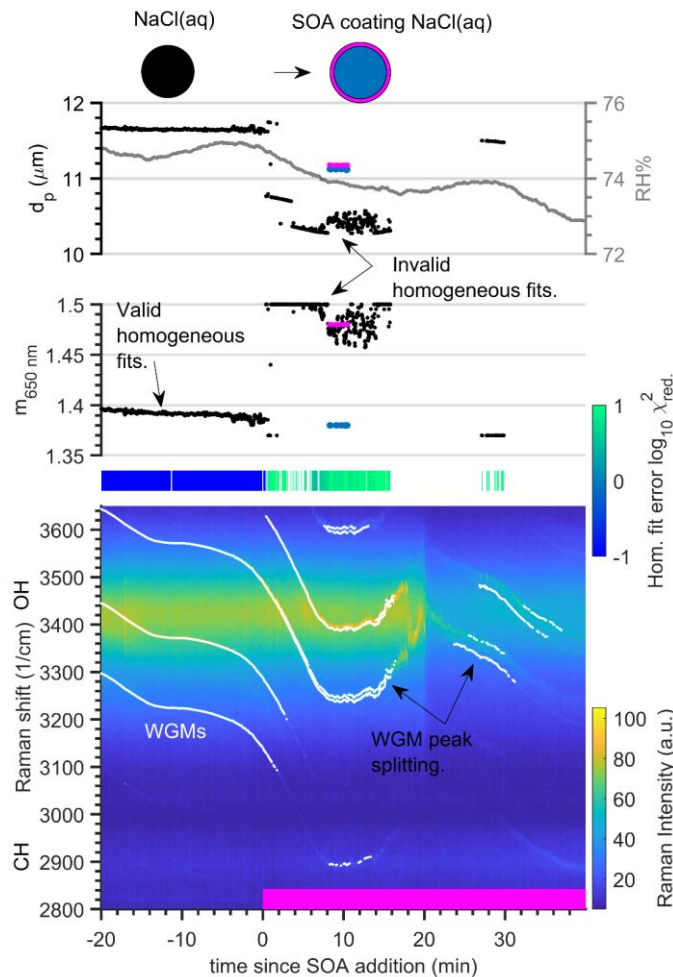


**Figure 6.** Raman spectral time series for a tweezed aqueous NaCl droplet with the addition of an  $\alpha$ -pinene SOA coating. Raman spectra are shown in the bottom graph, and the white points indicate the positions of detectable whispering gallery modes (WGMs). The decreasing slope of the WGM traces indicates the droplet is evaporating due to the RH decrease. The  $\alpha$ -pinene SOA flow reaction started at 0 min, indicated by the pink bar. The droplet's effective refractive index ( $m_{650\text{ nm}}$ ) and diameter ( $d_p$ ) retrieved every two seconds from the WGM analysis are shown in the middle and top panels. The RH is shown in the top right panel. The decrease in the diameter of the droplet following coating is due to a decrease in the RH of the chamber, causing evaporation of water. The fit results of the WGM positions to a homogeneous Mie model are in the top two panel as black dots. The fit error for the homogeneous model is shown in the green/blue bar, where consistently blue indicates a valid fit and green indicates an invalid fit to the model. The core-shell fitting is then used to retrieve the properties of the NaCl(aq) core (blue points) and  $\alpha$ -pinene SOA shell (pink points) at 10 min.

427 onto the trapped NaCl(aq) droplet. A detailed assessment of this aerosol system was  
 428 previously discussed in Gorkowski et al.<sup>24</sup> We use the core-shell fit results as guides for

1  
2  
3 429 this system due to the limited number of WGMs (6 per frame) and limited total number  
4  
5  
6 430 of frames (24) available to constrain the core-shell model. The retrieved refractive indices  
7  
8 431 are consistent with a NaCl(aq) core and SOA shell, when compared to our previous  
9  
10 432 work.<sup>24</sup> The retrieved shell thickness was ~25 nm, which highlights the resolving power  
11  
12 433 of the WGMs. In Figure 6 we should also note that the downward trend in WGM position  
13  
14 434 is also consistent with the decrease in size observed in the core-shell fit as well as the  
15  
16 435 decreasing RH. Lastly, the decreasing intensity of the WGMs after 15 minutes is  
17  
18 436 attributed to a formation of an emulsion of SOA in the aqueous NaCl core as discussed  
19  
20 437 in Gorkowski et al.<sup>24</sup>

### 21 438 **3.3 Evaporation of an Organic Carbon Core through an Organic Shell**

22  
23 439 We investigated our ability to measure phase-separated particles and the resulting  
24  
25 440 partitioning between the two phases using the coagulation of squalane ( $C_{30}H_{62}$ , a  
26  
27 441 hydrophobic long-chain hydrocarbon) onto an aqueous glycerol droplet. We observed  
28  
29 442 liquid-liquid phase-separation of these two compounds in beaker experiments, so we  
30  
31 443 expect phase-separation in the AOT. However, the actual morphology of the phase-  
32  
33 444 separated droplets remained unknown until our AOT experiments. The persistent  
34  
35 445 WGMs confirm a core-shell morphology (as opposed to a partially engulfing lens), with  
36  
37 446 glycerol forming the core.<sup>27,39</sup>

38  
39 447 In Figure 7 we show the core-shell fit results for an isolated part of the experiment  
40  
41 448 after we coagulated the squalane and coagulated additional glycerol to grow the droplet.  
42  
43 449 We used coagulative growth so that the droplet was large enough to identify more than  
44  
45 450 6 WGMs per frame. The fits shown in Figure 7 are for the 270 minutes (6603 spectral  
46  
47 451 frames) where the relative humidity (RH) was stable, and therefore composition was  
48  
49 452 constant. Under these stable RH conditions the core of the droplet is predominantly  
50  
51 453 glycerol, which continuously evaporates into the conditioned air due to its higher vapor  
52  
53 454 pressure; to a lesser extent the squalane shell also evaporates. This evaporation is  
54  
55 455 reflected in the fit as the diameter of the particle continuously decreases.

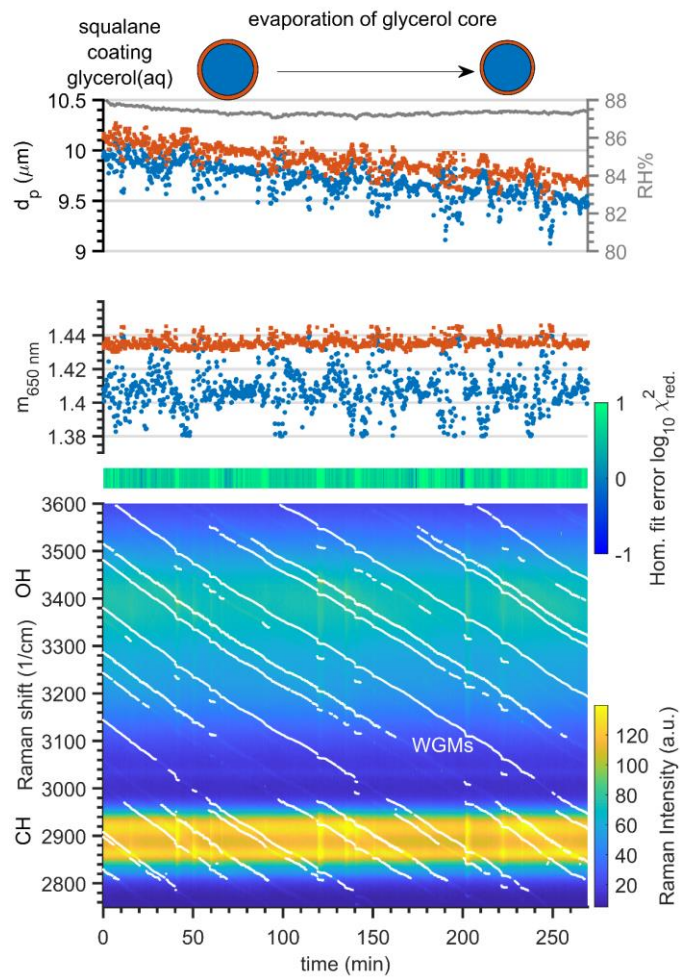


**Figure 7.** Raman spectral time series for a tweezed aqueous glycerol droplet coated with squalane. The evaporation of the glycerol core is observed from the decreasing trend in droplet diameter ( $d_p$ ). The panels follow the same format as in Fig. 6. The retrieved two-second Raman spectral frames are averaged to 15 seconds for clarity.

Our measurements are consistent with sparing but non-zero solubility of squalane and glycerol. The average shell refractive index,  $m_{650\text{nm}}$ , was  $1.4359 \pm 0.0042$  which is lower than pure squalane ( $m_{589\text{nm}} = 1.4474 \pm 0.0002^{55}$ ). This indicates a measurable amount of the aqueous glycerol absorbed in the squalane shell phase. Though our measured refractive index is at a different wavelength than the reference value, these should still be comparable given that the difference in wavelengths is small and as such the dispersion would only decrease the refractive index by  $\sim 0.001$  between 589 nm to 650 nm. The core is also not a just a glycerol and water solution as glycerol(aq). At 87.3% RH the pure

1  
2  
3 464 solution has mass fractions of 0.6 for  $w_{\text{water}}$  and 0.4 for  $w_{\text{glycerol}}$  resulting in an effective  
4  
5 465  $m_{589 \text{ nm}} = 1.384 \pm 0.008$ .<sup>56</sup> In contrast we observed a core with a higher effective refractive  
6  
7 466 index with at  $m_{650 \text{ nm}} = 1.4076 \pm 0.0128$  that must be due to mixing with squalane, which  
8  
9 467 would increase the effective refractive index. The higher uncertainty in  $m$  relative to the  
10  
11 468 simulated assessment (Fig. 7) is likely due to the simulation not matching the uncertainty  
12  
13 469 of determining the peak positions from the Raman spectrum.

14  
15 470 We have used this same fitting algorithm in our previous work on the mixing of  
16  
17 471 secondary organic aerosol phases with aqueous NaCl, aqueous glycerol and squalane<sup>24</sup>.  
18  
19 472 This algorithm allowed us to identify the morphology of the biphasic droplet and  
20  
21 473 determine the shell of SOA did not limit equilibration of the core. We are working  
22  
23 474 towards using the retrieved refractive indexes from the core-shell fitting to measure the  
24  
25 475 phase composition of both the core and the shell, to directly study phase partitioning and  
26  
27 476 solubility. Incorporation of a chemical thermodynamic equilibration model along with a  
28  
29 477 refractive index mixing model will extend this analysis to more components and complex  
30  
31 478 biphasic systems. With a method to determine the concentration of reactants we can  
32  
33 479 probe the feedback between chemical reaction rates, compositions, and morphology with  
34  
35 480 the biphasic system properties. This algorithm could probe the mechanisms behind the  
36  
37 481 salting out effect of polymers from an aqueous inorganic phase and the elucidate the  
38  
39 482 mechanisms behind the Hofmeister series that is widely-known in biochemical systems  
40  
41 483 for describing the salting-in/out of proteins.<sup>4</sup> Similarly, biphasic pH measurements could  
42  
43 484 be performed with a sufficiently accurate refractive index model.<sup>57</sup> The combined AOT  
44  
45 485 measurement system and new core-shell algorithm facilitates biphasic studies of  
46  
47 486 compounds in supersaturated inorganic solutions, which are often difficult to access  
48  
49 487 experimentally.<sup>27</sup> Understanding how biphasic systems evolve and their effects is an  
50  
51 488 active research topic in environmental chemistry, biochemistry, and atmospheric  
52  
53 489 chemistry.

54 490  
55  
56  
57  
58  
59  
60

## 491 4. Conclusions

492 We have developed a practical and efficient algorithm for fitting WGMs for a core-  
493 shell biphasic droplet. In the process, we have added to the understanding of how WGMs  
494 change as a second shell phase forms around a previously homogeneous trapped droplet.  
495 The major difference in WGMs in homogeneous and core-shell droplets is the peak  
496 splitting of adjacent WGMs which was predicted in Figure 2 and then demonstrated  
497 experimentally in Figure 6. We then tested our new fitting algorithm on simulated data  
498 for a homogeneous droplet achieving accuracies of  $\pm 4.6$  nm (0.045%) in particle diameter  
499 ( $d_p$ ) for a  $\sim 10$   $\mu$ m droplet and  $\pm 0.00067$  (0.058%) in refractive index ( $m$ ) for droplet with a  
500 refractive index of  $\sim 1.395$ . The same algorithm applied to a simulated core-shell droplet  
501 achieved accuracies of  $\pm 24$  nm (0.24%) in shell  $d_p$ ,  $\pm 359$  nm (3.8%) in core  $d_p$ , and  $\pm 0.0055$   
502 (0.37%) in core and shell refractive indices. Using our new algorithm, we analyzed an  
503 AOT experiment on a trapped core-shell droplet of squalane coating glycerol(aq). The  
504 retrieved refractive indices of the core and shell phases were used to inform the chemical  
505 composition of each phase. This improved efficient analysis method for core-shell  
506 droplets opens the door to future experiments that study the physicochemical properties  
507 and dynamics of biphasic droplets using aerosol optical tweezers, and the possibility for  
508 analysis in real-time.

509 **Conflicts of Interest.** There are no conflicts to declare.

510 **Acknowledgements.** This research was supported by the National Science Foundation  
511 (CHE-1554941). KG acknowledges support from the Bertucci Fellowship from the College  
512 of Engineering at Carnegie Mellon University. Jonathan Reid and James Walker at the  
513 University of Bristol provided valuable input regarding the evaluation of our new WGM  
514 fitting algorithm.

515 **References**

- 516 1 M. Iqbal, Y. Tao, S. Xie, Y. Zhu, D. Chen, X. Wang, L. Huang, D. Peng, A. Sattar, M.  
517 A. B. Shabbir, H. I. Hussain, S. Ahmed and Z. Yuan, Aqueous two-phase system  
518 (ATPS): an overview and advances in its applications, *Biol. Proced. Online*, 2016, **18**,  
519 1–18.
- 520 2 K. Mochizuki, T. Sumi and K. Koga, Liquid-liquid phase separation of N-  
521 isopropylpropionamide aqueous solutions above the lower critical solution  
522 temperature, *Sci. Rep.*, 2016, **6**, 1–10.
- 523 3 B. Monterroso, S. Zorrilla, M. Sobrinos-Sanguino, C. D. Keating and G. Rivas,  
524 Microenvironments created by liquid-liquid phase transition control the dynamic  
525 distribution of bacterial division FtsZ protein, *Sci. Rep.*, 2016, **6**, 1–13.
- 526 4 Y. Zhang and P. Cremer, Interactions between macromolecules and ions: the  
527 Hofmeister series, *Curr. Opin. Chem. Biol.*, 2006, **10**, 658–663.
- 528 5 B. Bagchi, Water Dynamics in the Hydration Layer around Proteins and Micelles,  
529 *Chem. Rev.*, 2005, **105**, 3197–3219.
- 530 6 J. Hirschfelder, D. Stevenson and H. Eyring, A Theory of Liquid Structure, *J. Chem.*  
531 *Phys.*, 1937, **5**, 896–912.
- 532 7 M. A. Freedman, Phase separation in organic aerosol, *Chem. Soc. Rev.*, 2017, **46**,  
533 7694–7705.
- 534 8 W. M. Aumiller and C. D. Keating, Experimental models for dynamic  
535 compartmentalization of biomolecules in liquid organelles: Reversible formation  
536 and partitioning in aqueous biphasic systems, *Adv. Colloid Interface Sci.*, 2017, **239**,  
537 75–87.
- 538 9 A. Abe, J. Genzer, W. H. De Jeu, S. Kobayashi, L. Leibler, T. E. Long, I. Manners, E.

- 1  
2  
3 539 M. Terentjev, M. Vicent, B. Voit, G. Wegner and U. Wiesner, *Self Organized*  
4 540 *Nanostructures of Amphiphilic Block Copolymers II*, Springer Berlin Heidelberg, Berlin,  
5 541 Heidelberg, 2011, vol. 242.  
6  
7  
8  
9  
10 542 10 C. Cai, D. J. Stewart, J. P. Reid, Y. Zhang, P. Ohm, C. S. Dutcher and S. L. Clegg,  
11 543 Organic Component Vapor Pressures and Hygroscopicities of Aqueous Aerosol  
12 544 Measured by Optical Tweezers, *J. Phys. Chem. A*, 2015, **119**, 704–718.  
13  
14  
15  
16 545 11 A. E. Haddrell, R. E. H. Miles, B. R. Bzdek, J. P. Reid, R. J. Hopkins and J. S. Walker,  
17 546 Coalescence Sampling and Analysis of Aerosols using Aerosol Optical Tweezers,  
18 547 *Anal. Chem.*, 2017, **89**, 2345–2352.  
19  
20  
21  
22  
23 548 12 J. F. Davies, A. E. Haddrell, A. M. J. Rickards and J. P. Reid, Simultaneous analysis  
24 549 of the equilibrium hygroscopicity and water transport kinetics of liquid aerosol.,  
25 550 *Anal. Chem.*, 2013, **85**, 5819–26.  
26  
27  
28  
29  
30 551 13 J. Buajarern, L. Mitchem and J. P. Reid, Characterizing the Formation of Organic  
31 552 Layers on the Surface of Inorganic/Aqueous Aerosols by Raman Spectroscopy, *J.*  
32 553 *Phys. Chem. A*, 2007, **111**, 11852–11859.  
33  
34  
35  
36 554 14 J. W. Lu, A. M. J. Rickards, J. S. Walker, K. J. Knox, R. E. H. Miles, J. P. Reid and R.  
37 555 Signorell, Timescales of water transport in viscous aerosol: measurements on sub-  
38 556 micron particles and dependence on conditioning history, *Phys. Chem. Chem. Phys.*,  
39 557 2014, **16**, 9819–9830.  
40  
41  
42  
43  
44 558 15 J. P. Reid, B. J. Dennis-Smith, N.-O. A. Kwamena, R. E. H. Miles, K. L. Hanford  
45 559 and C. J. Homer, The morphology of aerosol particles consisting of hydrophobic  
46 560 and hydrophilic phases: hydrocarbons, alcohols and fatty acids as the hydrophobic  
47 561 component., *Phys. Chem. Chem. Phys.*, 2011, **13**, 15559–15572.  
48  
49  
50  
51  
52  
53 562 16 B. J. Dennis-Smith, K. L. Hanford, N. A. Kwamena, R. E. H. Miles and J. P. Reid,  
54 563 Phase, morphology, and hygroscopicity of mixed oleic acid/sodium  
55  
56  
57  
58  
59  
60

- 1  
2  
3 564 chloride/water aerosol particles before and after ozonolysis., *J. Phys. Chem. A*, 2012,  
4 565 **116**, 6159–68.  
5  
6  
7  
8 566 17 A. M. J. Rickards, R. E. H. Miles, J. F. Davies, F. H. Marshall and J. P. Reid,  
9  
10 567 Measurements of the sensitivity of aerosol hygroscopicity and the  $\kappa$  parameter to  
11 568 the O/C ratio., *J. Phys. Chem. A*, 2013, **117**, 14120–31.  
12  
13  
14 569 18 B. J. Dennis-Smith, F. H. Marshall, R. E. H. Miles, T. C. Preston and J. P. Reid,  
15 570 Volatility and Oxidative Ageing of Aqueous Maleic Acid Aerosol Droplets and the  
16 571 Dependence on Relative Humidity., *J. Phys. Chem. A*, , DOI:10.1021/jp504823j.  
17  
18  
19  
20  
21 572 19 J. Buajarern, L. Mitchem and J. P. Reid, Characterizing Multiphase  
22 573 Organic/Inorganic/Aqueous Aerosol Droplets, *J. Phys. Chem. A*, 2007, **111**, 9054–  
23 574 9061.  
24  
25  
26  
27  
28 575 20 C. Cai, D. J. Stewart, T. C. Preston, J. S. Walker, Y. H. Zhang and J. P. Reid, A new  
29 576 approach to determine vapour pressures and hygroscopicities of aqueous aerosols  
30 577 containing semi-volatile organic compounds., *Phys. Chem. Chem. Phys.*, 2014, **16**,  
31 578 3162–72.  
32  
33  
34  
35  
36 579 21 T. C. Preston and J. P. Reid, Accurate and efficient determination of the radius,  
37 580 refractive index, and dispersion of weakly absorbing spherical particle using  
38 581 whispering gallery modes, *J. Opt. Soc. Am. B-Optical Phys.*, 2013, **30**, 2113–2122.  
39  
40  
41  
42  
43 582 22 R. Power, J. P. Reid, S. Anand, D. McGloin, a Almohammed, a Almohamed, N.  
44 583 S. Mistry and a J. Hudson, Observation of the binary coalescence and equilibration  
45 584 of micrometer-sized droplets of aqueous aerosol in a single-beam gradient-force  
46 585 optical trap., *J. Phys. Chem. A*, 2012, **116**, 8873–84.  
47  
48  
49  
50  
51 586 23 A. Moridnejad, T. C. Preston and U. K. Krieger, Tracking Water Sorption in Glassy  
52 587 Aerosol Particles using Morphology-Dependent Resonances, *J. Phys. Chem. A*, 2017,  
53 588 **121**, 8176–8184.  
54  
55  
56  
57  
58  
59  
60

- 1  
2  
3 589 24 K. Gorkowski, N. M. Donahue and R. C. Sullivan, Emulsified and Liquid-Liquid  
4 590 Phase-Separated States of  $\alpha$ -Pinene Secondary Organic Aerosol Determined Using  
5 591 Aerosol Optical Tweezers, *Environ. Sci. Technol.*, 2017, **51**, 12154–12163.  
6  
7  
8  
9  
10 592 25 G. Hargreaves, N.-O. Kwamena, Y. H. Zhang, J. R. Butler, S. Rushworth, S. L.  
11 593 Clegg and J. P. Reid, Measurements of the equilibrium size of supersaturated  
12 594 aqueous sodium chloride droplets at low relative humidity using aerosol optical  
13 595 tweezers and an electrodynamic balance., *J. Phys. Chem. A*, 2010, **114**, 1806–15.  
14  
15  
16  
17  
18 596 26 B. R. Bzdek, L. Collard, J. E. Sprittles, A. J. Hudson and J. P. Reid, Dynamic  
19 597 measurements and simulations of airborne picolitre-droplet coalescence in  
20 598 holographic optical tweezers, *J. Chem. Phys.*, 2016, **145**, 054502.  
21  
22  
23  
24  
25 599 27 K. Gorkowski, H. Beydoun, M. Aboff, J. S. Walker, J. P. Reid and R. C. Sullivan,  
26 600 Advanced aerosol optical tweezers chamber design to facilitate phase-separation  
27 601 and equilibration timescale experiments on complex droplets, *Aerosol Sci. Technol.*,  
28 602 2016, **50**, 1327–1341.  
29  
30  
31  
32  
33 603 28 R. M. Power and J. P. Reid, Probing the micro-rheological properties of aerosol  
34 604 particles using optical tweezers, *Reports Prog. Phys.*, 2014, **77**, 074601.  
35  
36  
37  
38 605 29 R. E. H. Miles, J. S. Walker, D. R. Burnham and J. P. Reid, Retrieval of the complex  
39 606 refractive index of aerosol droplets from optical tweezers measurements, *Phys.*  
40 607 *Chem. Chem. Phys.*, 2012, **14**, 3037.  
41  
42  
43  
44  
45 608 30 J. S. Walker, J. B. Wills, J. P. Reid, L. Wang, D. O. Topping, J. R. Butler and Y.-H.  
46 609 Zhang, Direct comparison of the hygroscopic properties of ammonium sulfate and  
47 610 sodium chloride aerosol at relative humidities approaching saturation., *J. Phys.*  
48 611 *Chem. A*, 2010, **114**, 12682–12691.  
49  
50  
51  
52  
53 612 31 B. J. Mason, S.-J. King, R. E. H. Miles, K. M. Manfred, A. M. J. Rickards, J. Kim, J. P.  
54 613 Reid and A. J. Orr-Ewing, Comparison of the accuracy of aerosol refractive index  
55  
56  
57  
58  
59  
60

- 1  
2  
3 614 measurements from single particle and ensemble techniques., *J. Phys. Chem. A*,  
4 615 2012, **116**, 8547–56.  
5  
6  
7  
8 616 32 T. C. Preston and J. P. Reid, Determining the size and refractive index of  
9 617 microspheres using the mode assignments from Mie resonances, *J. Opt. Soc. Am. A*,  
10 618 2015, **32**, 2210–2217.  
11  
12  
13  
14 619 33 N.-O. A. Kwamena, J. Buajarern and J. P. Reid, Equilibrium morphology of mixed  
15 620 organic/inorganic/aqueous aerosol droplets: investigating the effect of relative  
16 621 humidity and surfactants., *J. Phys. Chem. A*, 2010, **114**, 5787–95.  
17  
18  
19  
20  
21 622 34 R. E. O'Brien, B. Wang, S. T. Kelly, N. Lundt, Y. You, A. K. Bertram, S. R. Leone, A.  
22 623 Laskin, M. K. Gilles, R. E. O'Brien, B. Wang, S. T. Kelly, N. Lundt, Y. You, A. K.  
23 624 Bertram, S. R. Leone, A. Laskin and M. K. Gilles, Liquid–Liquid Phase Separation  
24 625 in Aerosol Particles: Imaging at the Nanometer Scale, *Environ. Sci. Technol.*, 2015,  
25 626 **49**, 4995–5002.  
26  
27  
28  
29  
30  
31 627 35 Y. You, M. L. Smith, M. Song, S. T. Martin and A. K. Bertram, Liquid–liquid phase  
32 628 separation in atmospherically relevant particles consisting of organic species and  
33 629 inorganic salts, *Int. Rev. Phys. Chem.*, 2014, **33**, 43–77.  
34  
35  
36  
37  
38 630 36 M. Shiraiwa, A. Zuend, A. K. Bertram and J. H. Seinfeld, Gas-particle partitioning  
39 631 of atmospheric aerosols: interplay of physical state, non-ideal mixing and  
40 632 morphology., *Phys. Chem. Chem. Phys.*, 2013, **15**, 11441–53.  
41  
42  
43  
44 633 37 L. Renbaum-Wolff, M. Song, C. Marcolli, Y. Zhang, P. F. Liu, J. W. Grayson, F. M.  
45 634 Geiger, S. T. Martin and A. K. Bertram, Observations and implications of liquid–  
46 635 liquid phase separation at high relative humidities in secondary organic material  
47 636 produced by *a*-pinene ozonolysis without inorganic salts, *Atmos. Chem. Phys.*, 2016,  
48 637 **16**, 7969–7979.  
49  
50  
51  
52  
53  
54  
55 638 38 U. K. Krieger, C. Marcolli and J. P. Reid, Exploring the complexity of aerosol  
56  
57  
58  
59  
60

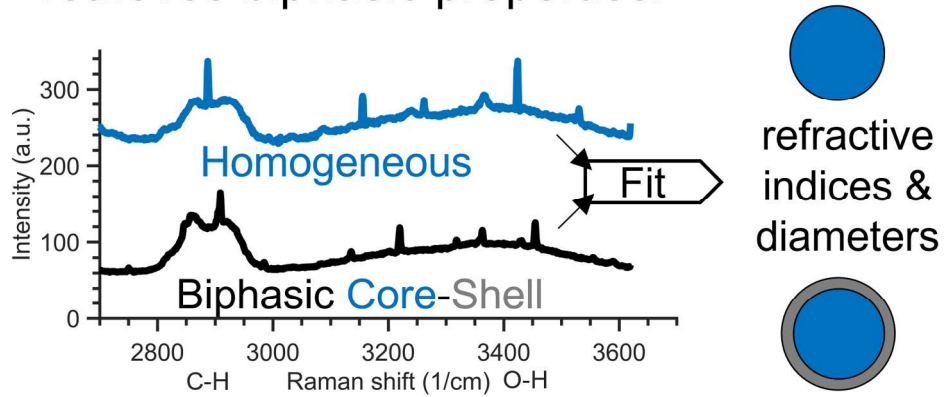
- 1  
2  
3 639 particle properties and processes using single particle techniques, *Chem. Soc. Rev.*,  
4 640 2012, **41**, 6631.  
5  
6  
7  
8 641 39 D. J. Stewart, C. Cai, J. Naylor, T. C. Preston, J. P. Reid, U. K. Krieger, C. Marcolli  
9  
10 642 and Y.-H. H. Zhang, Liquid-Liquid Phase Separation in Mixed Organic/Inorganic  
11 643 Single Aqueous Aerosol Droplets, *J. Phys. Chem. A*, 2015, **119**, 4177–4190.  
12  
13  
14 644 40 D. J. Stewart, C. Cai, J. Naylor, T. C. Preston, J. P. Reid, U. K. Krieger, C. Marcolli  
15 645 and Y. H. Zhang, Liquid-Liquid Phase Separation in Mixed Organic/Inorganic  
16 646 Single Aqueous Aerosol Droplets, *J. Phys. Chem. A*, 2015, **119**, 4177–4190.  
17  
18  
19  
20  
21 647 41 A. Zuend and J. H. Seinfeld, A practical method for the calculation of liquid-liquid  
22 648 equilibria in multicomponent organic-water-electrolyte systems using  
23 649 physicochemical constraints, *Fluid Phase Equilib.*, 2013, **337**, 201–213.  
24  
25  
26  
27  
28 650 42 J. Ovadnevaite, A. Zuend, A. Laaksonen, K. J. Sanchez, G. Roberts, D. Ceburnis, S.  
29 651 Decesari, M. Rinaldi, N. Hodas, M. C. Facchini, J. H. Seinfeld and C. O' Dowd,  
30 652 Surface tension prevails over solute effect in organic-influenced cloud droplet  
31 653 activation, *Nature*, 2017, **546**, 637–641.  
32  
33  
34  
35  
36 654 43 A. Zuend and J. H. Seinfeld, Modeling the gas-particle partitioning of secondary  
37 655 organic aerosol: The importance of liquid-liquid phase separation, *Atmos. Chem.*  
38 656 *Phys.*, 2012, **12**, 3857–3882.  
39  
40  
41  
42  
43 657 44 A. Zuend, C. Marcolli, A. M. Booth, D. M. Lienhard, V. Soonsin, U. K. Krieger, D.  
44 658 O. Topping, G. McFiggans, T. Peter and J. H. Seinfeld, New and extended  
45 659 parameterization of the thermodynamic model AIOMFAC: Calculation of activity  
46 660 coefficients for organic-inorganic mixtures containing carboxyl, hydroxyl,  
47 661 carbonyl, ether, ester, alkenyl, alkyl, and aromatic functional groups, *Atmos. Chem.*  
48 662 *Phys.*, 2011, **11**, 9155–9206.  
49  
50  
51  
52  
53  
54  
55 663 45 A. K. Ray and R. Nandakumar, Simultaneous determination of size and  
56  
57  
58  
59  
60

- 1  
2  
3 664 wavelength-dependent refractive indices of thin-layered droplets from optical  
4  
5 665 resonances., *Appl. Opt.*, 1995, **34**, 7759–7770.  
6  
7  
8 666 46 O. B. Toon and T. P. Ackerman, Algorithms for the calculation of scattering by  
9  
10 667 stratified spheres, *Appl. Opt.*, 1981, **20**, 3657–3660.  
11  
12  
13 668 47 J. B. Snow, S. X. Qian and R. K. Chang, Stimulated Raman scattering from  
14  
15 669 individual water and ethanol droplets at morphology-dependent resonances., *Opt.*  
16  
17 670 *Lett.*, 1985, **10**, 37–39.  
18  
19  
20 671 48 J. Popp, M. Lankers, K. Schaschek, W. Kiefer and J. T. Hodges, Observation of  
21  
22 672 sudden temperature jumps in optically levitated microdroplets due to  
23  
24 673 morphology-dependent input resonances., *Appl. Opt.*, 1995, **34**, 2380–6.  
25  
26  
27 674 49 J. F. Owen, P. W. Barber, B. J. Messinger and R. K. Chang, Determination of optical-  
28  
29 675 fiber diameter from resonances in the elastic scattering spectrum, *Opt. Lett.*, 1981,  
30  
31 676 **6**, 272.  
32  
33  
34 677 50 V. S. Ilchenko, A. a Savchenkov, A. B. Matsko and L. Maleki, Dispersion  
35  
36 678 compensation in whispering gallery modes, *J. Opt. Soc. Am. A*, 2003, **20**, 157–162.  
37  
38  
39 679 51 S. C. Hill, C. K. Rushforth, R. E. Benner and P. R. Conwell, Sizing dielectric spheres  
40  
41 680 and cylinders by aligning measured and computed resonance locations: algorithm  
42  
43 681 for multiple orders, *Appl. Opt.*, 1985, **24**, 2380.  
44  
45  
46 682 52 R. L. Hightower and C. B. Richardson, Resonant Mie scattering from a layered  
47  
48 683 sphere., *Appl. Opt.*, 1988, **27**, 4850–5.  
49  
50  
51 684 53 C. F. Bohren and D. R. Huffman, *Absorption and Scattering of Light by Small Particles*,  
52  
53 685 Wiley-VCH Verlag GmbH, Weinheim, Germany, 1998.  
54  
55  
56 686 54 P. R. Conwell, C. K. Rushforth, R. E. Benner and S. C. Hill, Efficient automated  
57  
58 687 algorithm for the sizing of dielectric microspheres using the resonance spectrum, *J.*

- 1  
2  
3 688 *Opt. Soc. Am. A*, 1984, **1**, 1181.  
4  
5  
6 689 55 G. P. Dubey, N. Tripathi and S. C. Bhatia, Refractive index of ternary liquid systems  
7  
8 690 of squalane (+ hexane + benzene; + cyclohexane + benzene and + hexane +  
9  
10 691 cyclohexane), *Indian J. Pure Appl. Phys.*, 2005, **43**, 175–179.  
11  
12  
13 692 56 Haynes W. M., *CRC Handbook of Chemistry and Physics*, 97th Edition, 2017.  
14  
15 693 57 D. J. Losey, R. G. Parker and M. A. Freedman, pH Dependence of Liquid–Liquid  
16  
17 694 Phase Separation in Organic Aerosol, *J. Phys. Chem. Lett.*, 2016, **7**, 3861–3865.  
18  
19

20 695  
21  
22  
23  
24  
25  
26  
27  
28  
29  
30  
31  
32  
33  
34  
35  
36  
37  
38  
39  
40  
41  
42  
43  
44  
45  
46  
47  
48  
49  
50  
51  
52  
53  
54  
55  
56  
57  
58  
59  
60

Algorithm to fit Whispering Gallery Modes retrieves biphasic properties.



528x263mm (96 x 96 DPI)